Research Article

Nano Research
2022, 15(6): 4958–4964

ISSN 1998-0124 CN 11-5974/O4
https://doi.org/10.1007/s12274-022-4128-6

Reduced water dissociation barrier on constructing Pt-Co/CoO_x interface for alkaline hydrogen evolution

Yandong Wang[1], Wei Wu[1], Runzhe Chen[1], Caoxin Lin[1], Shichun Mu[2], and Niancai Cheng[1] (✉)

[1] College of Materials Science and Engineering, Fuzhou University, Fuzhou 350108, China
[2] State Key Laboratory of Advanced Technology for Materials Synthesis and Processing, Wuhan University of Technology, Wuhan 430070, China

Received: 10 December 2021 / **Revised:** 29 December 2021 / **Accepted:** 30 December 2021

ABSTRACT

Water dissociation process is generally regarded as the rate-limiting step for alkaline hydrogen evolution reaction (HER), and severely inhibits the catalytic efficiency of Pt based catalysts. To overcome this problem, the *in-situ* constructed interfaces of Pt-Co alloy and amorphous cobalt oxide (CoO_x) on the carbon powder are designed. The amorphous CoO_x at Pt-Co/CoO_x interfaces not only provide active sites for water dissociation to facilitate Volmer step, but also produce the strong electronic transfer with Pt-Co. Accordingly, the obtained interfacial catalysts exhibit outstanding alkaline HER performance with a Tafel slope of 29.3 mV·dec^{-1} and an ultralow overpotential of only 28 mV at 10 mA·cm^{-2}. Density functional theory (DFT) reveals that the electronic accumulation on the interfacial Co atom in Pt-Co/CoO_x constructing the novel active site for water dissociation. Compared to the Pt-Co, all of the energy barriers for water adsorption, water dissociation and hydrogen adsorption/desorption are reduced in Pt-Co/CoO_x interfaces, suggesting a boosted HER kinetics for alkaline HER.

KEYWORDS

interfacial construction, amorphous cobalt oxide, water dissociation, dual active site, electronic regulation

1 Introduction

The inherently sluggish kinetics at cathodic hydrogen evolution reaction (HER), originated from the scarcity of free hydrogen ions in alkaline electrolytes, hinder the industrial alkaline electrolyte application [1–4]. Thus, designing highly efficient catalysts to favor HER is a significant need for accelerating the alkaline electrolyte industry. Typically, platinum-based materials as the state of the art HER electrocatalysts show much lower reaction efficiency for alkaline HER due to the sluggish kinetics in the Volmer step ($H_2O + * + e^- \rightarrow H^* + OH^-$) [5–9]. The formation of Pt-H_{ab} band is harsh and hinders the subsequent process of hydrogen adsorption/desorption in the alkaline media [10–12]. Therefore, rationally optimizing water dissociation is very important for Pt-based catalyst to improve the alkaline catalytic behavior.

Pt-based transition metal alloys have been proved as an efficient strategy to improve alkaline HER activity through facilitating water dissociation [13–16]. The introduced transition metals (Co, Ni, Fe, Cu, etc.) not only generate the adsorption sites for OH^- derived from the optimized appreciate oxytropism, but also provide electrons for Pt and regulate the electronic structures [17–20]. Due to the lattice mismatch between transition metals and Pt, the 3d states of the transition metals will be narrowed and the d band of Pt will be lower, which contribute to the water coupling and optimize the hydrogen binding energy to accelerate hydrogen coupling process [21–25].

Additionally, constructing interface with transition metal oxides (TMO) has also been demonstrated as another effective route to enhance the water dissociation ability of Pt based catalysts [26, 27]. The dual active sites at the interface allow the separate reaction steps to successively occur on adjacent sites during the alkaline HER process [28, 29], which preferentially adsorbing the water molecule on the TMO sites to proceed water dissociation step with the lower energy barriers [30, 31], and subsequently coupling the dissociated H* with Pt sites for the hydrogen adsorption/desorption process. Moreover, the strong electronic transfer between Pt and TMO at the interface will not only regulate the electronic configuration [32, 33], but also provide the reconstructed active center at the interface [34–36], which both increasing the intrinsic activity for water dissociation of catalysts.

Among the various TMOs, the amorphous cobalt oxide (CoO_x) with the characters of metastable structure, disordered long-range atomic arrangement and accommodating inherent abundant defects exhibit advantage of flexibility, which allow CoO_x self-regulating into higher active sites in the different electrocatalytic condition and thus exhibit higher intrinsic catalytic activity than the crystalline counterparts in various electrocatalytic reactions [37–40]. Besides, randomly orient bonds and flexible structure of the CoO_x result in the abundant defects and unsaturated sites, which facilitate the adsorption of reactants and further enhance the catalytic activity [41–43].

Herein, by *in-situ* constructing the interface between Pt-Co alloy and amorphous CoO_x, we have successfully designed a highly efficient Pt-Co/CoO_x/C catalyst with enhanced water dissociated ability. The Pt-Co/CoO_x interfacial structure was achieved through annealing the Pt-Co/C in air atmosphere with the controlled heating duration, which leads to the generation of

Address correspondence to niancaicheng@fzu.edu.cn

amorphous CoO_x around Pt-Co and realize the *in-situ* construction of Pt-Co/CoO_x interface. Benefiting from the dual active sites and strong electronic transfer at the interfaces, the prepared Pt-Co/CoO_x/C catalyst exhibit excellent alkaline HER activity with an ultralow overpotential of 28 mV at 10 mV·cm^{-2}. The theoretical analysis further revealed that the string electronic transfer at Pt-Co/CoO_x interface will result in the electronic accumulation at interfacial Co sites between amorphous cobalt oxide and Pt-Co alloy, constructing a novel active site. The interfacial Co site not only facilitate the adsorption of water molecule, but also exhibit the reduced barriers for the dissociation from water to H* and OH*, leading to the much higher catalytic activity for the water dissociation step in alkaline HER. Moreover, the Pt sites nearby the interfacial Co also exhibit the more ideal hydrogen binding energy than that in pristine Pt-Co structure. Accordingly, the kinetically sluggish multi-step reactions of alkaline can be efficiently facilitated by the construction of Pt-Co/CoO_x interface, which providing a highly efficient approach to enhance the water dissociated ability for Pt-based catalysts.

2 Experimental

2.1 Materials

Hexahydrate chloroplatinic acid ($H_2PtCl_6·6H_2O$), ethylene glycol (EG), cobalt nitrate hexahydrate ($Co(NO_3)_2·6H_2O$), sodium hydroxide (NaOH), and isopropyl alcohol were purchased from Sinopharm Chemical Reagent Co., Ltd. XC-72R carbon black and Nafion were purchased from Cobot Corporation. All these materials were used as received.

2.2 Preparation methods

Pt-Co/CoO_x/C: The precursors Pt-Co/C-H was firstly synthesized by polyol process [44, 45] as follows: 4.98 mL $H_2PtCl_6·6H_2O$ (8 mg/mL), 11.19 mg $Co(NO_3)_2·6H_2O$, 60 mg XC-72R carbon black, and 150 mg NaOH were mixed into 150 mL EG, and refluxing the mixture at 220 °C for 4 h. By the following filtration, deionized water washing, and dried, the products Pt-Co/C were obtained and then annealed in the under 10% H_2 /90% N_2 atmosphere at 250 °C for 1 h to obtain the Pt-Co/C-H catalyst. Finally, the as-prepared Pt-Co/C-H catalyst was treated at 200 °C under air atmosphere for 15, 30, and 60 min donated as Pt-Co/C-HA_{15}, Pt-Co/C-HA_{30}, and Pt-Co/C-HA_{60}, respectively.

2.3 Characterizations

The electrocatalytic HER were performed by a three-electrodes setup on Autolab electrochemical workstation. The working electrodes were prepared by depositing 5 μL catalyst ink, which was prepared by ultrasonicated mixing 4 mg of catalyst in 1 mL deionized (DI) water and 1 mL isopropyl alcohol and 20 μL Nafion (5 wt.%). Meanwhile, graphite rod and Ag/AgCl electrode were used as counter electrode and reference electrode, respectively. At the beginning of HER test, Ar gas was aerated into KOH electrolyte for 30 min and 20 cyclic voltammetry (CV) cycles were applied on working electrode from −0.3 to 0 V to stabilize the catalyst. The linear sweep voltammetry (LSV) were recorded at a scan rate of 5 mV·s^{-1}. Electrochemical impedance spectroscopy (EIS) was performed in a frequency range from 100 kHz to 0.01 Hz. Turnover frequency (TOF) was obtained from the following equation: $I/2nF$; I is the current, F is the Faraday constant (96,485.3 C·mol^{-1}), and n is the number of moles of the active catalyst. All these results were obtained by *iR*-compensation, and all potentials were determined with respect to RHE using the equation: $E_{RHE} = E_{Ag/AgCl} + E^0_{Ag/AgCl} + 0.0592 \times pH$.

2.4 Theoretical calculations

Theoretical calculations were investigated using Vienna *ab initio* simulation package (VASP) based on density functional theory (DFT). Projector-augmented wave (PAW) potentials were used to simulate the interaction between valence electrons and nuclei. Additionally, Perdew–Burker–Ernzerhof (PBE) and generalized gradient approximation (GGA) using exchange correlation functions were used to study electron transfer and interrelationships. The cut-off energy of plane waves was at 400 eV. The Gaussian dispersion width of 0.2 eV was applied to meet the occupancy. The maximum force and energy of unconstrained atoms were limited to 0.01 eV/Å and 1×10^{-6} eV, respectively. The Brillouin zone was sampled by $3 \times 3 \times 1$ Monhorst–Pack *k*-point meshes.

3 Results and discussion

3.1 Synthesis and structure characterization

The hybrid Pt-Co/CoO_x/C electrocatalyst composing of interfacial Pt-Co/CoO_x on the carbon powders was synthesized by an *in-situ* oxidation treatment as illustrated in Scheme 1. Namely, the Pt-Co alloy nanoparticles anchored on the C powder (Pt-Co/C) were synthesized as the precursors through EG reducing reaction and Ar/H_2 annealing. By following annealing Pt-Co/C-H in the air environment, the Co elements in the alloy will be oxidized into oxide cobalt and precipitates out from the surface of Pt-Co, which constructing the interface between oxide cobalt and Pt-Co. Through the regulation of the heating duration, the atomic arrangement of oxide cobalt can be well controlled into amorphization, and achieving the target catalyst Pt-Co/CoO_x/C. Examined by the inductively coupled plasma (Table S1 in the Electronic Supplementary Material (ESM)), the Pt-loading contents was 15.1% after EG reducing reaction and Ar/H_2 annealing. The construction and structural evolution of Pt-Co/CoO_x interface was observed by transmission electron microscopy (TEM). A uniform distribution of crystal nanoparticles on the pristine Pt-Co/C (Fig. S1 in the ESM) can be observed on carbon with an average size of 2.0 nm. Meanwhile, crystalline nanoparticles exhibit the interplanar spacing of 0.219 nm belong to the (111) plane of Pt, which demonstrating the successful synthesis of Pt-Co alloy nanoparticles on carbon. After annealing Pt-Co/C in Ar/H_2 atmosphere (Figs. 1(a)–1(c)), no significant change can be observed on the morphology and the average particle size around 2 nm of Pt-Co alloy maintained. For the 15 min annealed catalyst (Pt-Co/C-HA_{15}), it can be observed that some nanoparticles without lattice fringes were generated on the surface of partial Pt-Co alloy (Fig. 1(d)), which are regarded as the amorphous CoO_x nanoparticles. The generated CoO_x nanoparticles were closely interconnected with the Pt-Co alloy, and spontaneously constructing the Pt-Co/CoO_x interface. When

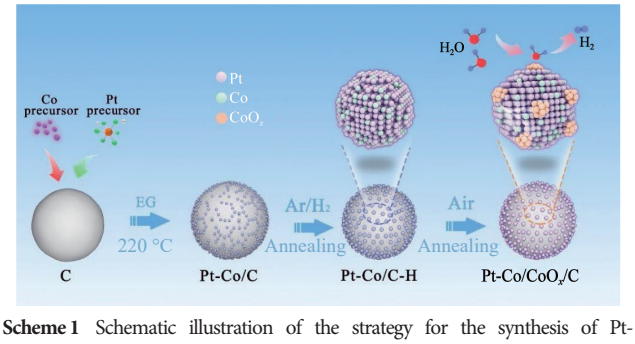

Scheme 1 Schematic illustration of the strategy for the synthesis of Pt-Co/CoO_x/C.

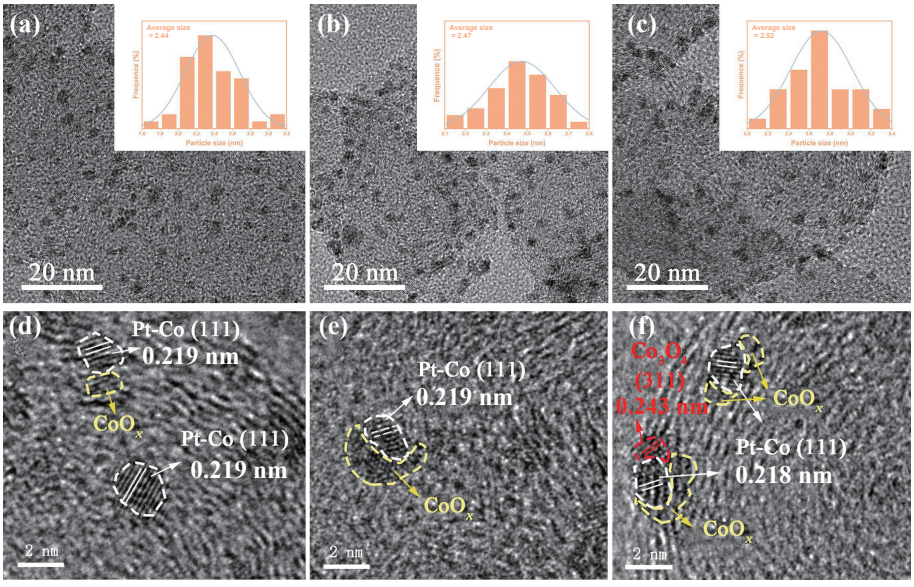

Figure 1 TEM and HRTEM images of (a) and (d) Pt-Co/C-HA$_{15}$ catalysts, (b) and (e) Pt-Co/C-HA$_{30}$ catalysts, and (c) and (f) Pt-Co/C-A$_{60}$ catalysts.

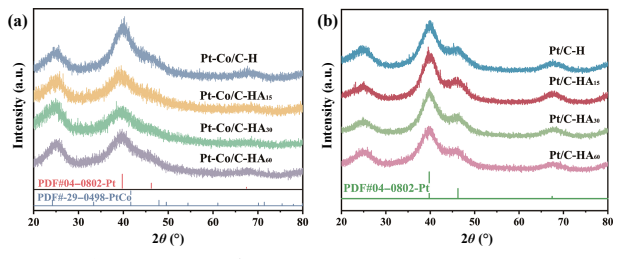

Figure 2 (a) XRD patterns of Pt-Co/C-H, Pt-Co/C-HA$_{15}$, Pt-Co/C-HA$_{30}$, and Pt-Co/C-HA$_{60}$ catalysts. (b) XRD patterns of Pt/C-H, Pt/C-HA$_{15}$, Pt/C-HA$_{30}$, and Pt/C-HA$_{60}$ catalysts.

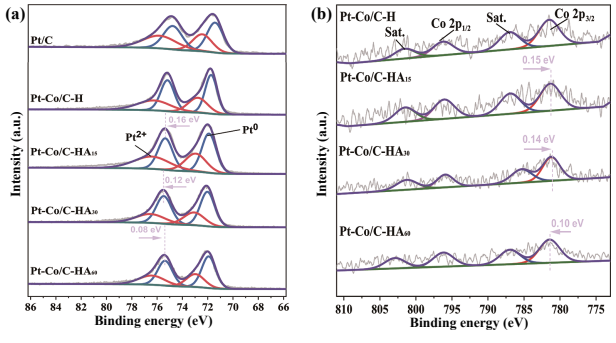

Figure 3 XPS of spectra of (a) Pt 4f and (b) Co 2p for Pt/c, Pt-Co/C-H, Pt-Co/C-HA$_{15}$, Pt-Co/C-HA$_{30}$, and Pt-Co/C-HA$_{60}$ catalysts.

the annealing time prolong to 30 min (Pt-Co/C-HA$_{30}$), the generation of amorphous CoO$_x$ nanoparticles significantly increased, and the Pt-Co/CoO$_x$ interface were constructed around almost all Pt-Co alloy particles (Fig. 1(e)). When the annealing time further prolonged and reached 1 h, the interplanar spacing of 0.243 nm began to form in partial CoO$_x$ nanoparticles, which can be attributed to the (311) plane of Co_3O_4, indicating that partial amorphous CoO$_x$ nanoparticles began to be further oxidized into the crystalline Co_3O_4 nanoparticles (Fig. 1(f)). The result of TEM images clearly showed a progressively *in-situ* constructed process of Pt-Co/CoO$_x$ interface, and reveal that the control of annealing duration is the key for forming amorphous CoO$_x$. Moreover, the structural evolution of Pt-Co/C samples can also be reflected by X-ray diffraction (XRD). In Fig. 2(a), the characteristic peak to the Pt-Co alloy in Pt-Co/C was significantly weakened after annealing in air atmosphere. While for the Pt/C, no significant change can be observed on the characteristic peak of Pt (111) after the same annealing process (Fig. 2(b)). This change in Pt-Co/C can be attributed to the precipitation of cobalt ions in alloy during the formation of CoO$_x$, which destroys the crystallinity of Pt-Co alloy [46].

To investigate the chemical status and electronic structure on the Pt-Co/CoO$_x$ interfaces, the X-ray photoelectron spectroscopy (XPS) measurements are performed. As shown in the high-resolution Pt 4f spectrum (Fig. 3(a) and Table S2 in the ESM), the signals located at 71.43/74.77 and 72.44/75.83 eV in Pt/C were ascribed to the Pt^0 and Pt^{2+} species, respectively [47–49]. In the Pt-Co/C-H, the Pt 4f peaks show a positive shift of 0.31 eV by the alloying of Pt-Co. While for the Pt-Co/C-HA$_{15}$, the Pt 4f peaks show a positive shift of 0.16 eV, which can be attributed to the formation of amorphous cobalt oxide. When the annealing duration prolong to 30 min and constructing more Pt-Co/CoO$_x$ interface, the positive shift of Pt 4f peaks further increased 0.12 eV. While for the 1 h annealed Pt-Co/C-HA$_{60}$, a negative shift of 0.08 eV was occurred on the Pt 4f peaks compare to Pt-Co/C-HA$_{30}$, due to the crystallization from CoO$_x$ to Co_3O_4. Meanwhile, the high-resolution Co 2p spectrum shows the corresponding results in Fig. 3(b) and Table S3 in the ESM. When annealing Pt-Co/C-H for 15 and 30 min, the binding energy of Co 2p signals negatively shifted 0.15 and 0.29 eV, and a positive shift of 0.10 eV can be observed when the annealing duration prolonged from 30 to 60 min. The shift of binding energy in Co 2p and Pt 4f indicate that the electrons will transfer from strong Pt to Co by constructing the interface between Pt-Co alloy and oxide cobalt, and the amorphous CoO$_x$ exhibit the much stronger electronic interaction with Pt-Co compare to the crystalline Co_3O_4.

3.2 HER catalytic activity

The HER performance of as-prepared catalysts is evaluated in Ar-saturated 1 M KOH. As shown in the Fig. 4(a), the Pt-Co/C-H shows superior HER performance with the low overpotential of 46 mV, much lower than that of Pt/C (72 mV), indicating that alloying with Co can efficiently improve the Pt activity towards HER. The constructed the interface on Pt-Co alloy will enhance the HER activity. The overpotential at 10 mA·cm^{-2} decreased to 40 mV in Pt-Co/C-HA$_{15}$, and further improved to 28 mV with the more interfacial construction on Pt-Co/C-HA$_{30}$, which makes it as a promising electrocatalysts compared with recently reported Pt based electrocatalysts for alkaline HER (Table S4 in the ESM). While for the Pt-Co/C-HA$_{60}$, the catalytic activity for HER instead degrades, and the overpotential is 35 mV, larger than that of Pt-

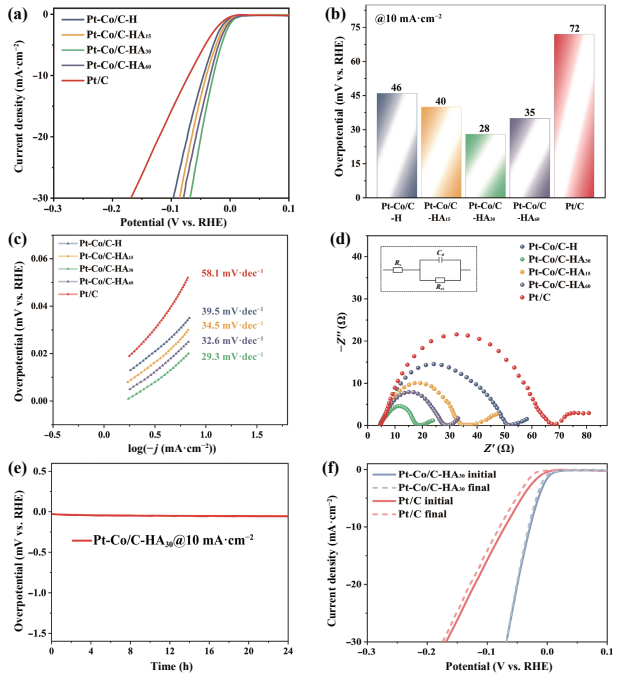

Figure 4 (a) HER polarization curves. (b) Overpotential at 10 mA·cm^{-2}. (c) Tafel plots for Pt-Co/C-H, Pt-Co/C-HA$_{15}$, Pt-Co/C-HA$_{30}$, Pt-Co/C-HA$_{60}$, and Pt/C catalysts in 1 M KOH. (d) Nyquist plots at the overpotential of 30 mV vs. RHE in 1 M KOH in the frequency range of 100 kHz to 0.01 Hz. Insert: the fitting circuit. (e) Chronopotentiometry curve of Pt-Co/C-HA$_{30}$ at 10 mA·cm^{-2}. (f) HER polarization curves for Pt-Co/C-HA$_{30}$ and Pt/C before and after 1,000 cyclic voltammetry cycles.

Co/C-HA$_{30}$. TOF values of the catalysts were calculated from LSV curves and displayed in Fig. S2 in the ESM. Pt-Co/C-HA$_{30}$ exhibits a TOF of 1.38 s^{-1} at an overpotential of 50 mV, which is about 1.23, 1.5, 1.79, 2.26, and 5.1 times higher than those of Pt-Co/C-HA$_{60}$ (1.12 s^{-1}), Pt-Co/C-HA$_{15}$ (0.92 s^{-1}), Pt-Co/C-H (0.77 s^{-1}), Pt-Co/C (0.61 s^{-1}), and Pt/C (0.27 s^{-1}), respectively. Moreover, Fig. S3 in the ESM shows the mass activity of as-prepared catalysts at the overpotential of 50 mV. The Pt-Co/C-HA$_{30}$ also presents the highest HER mass activity of 1.36 A·mg^{-1}, which is 1.79, 1.49, 1.23, and 5.04 times of Pt-Co/C-H (0.76 A·mg^{-1}), Pt-Co/C-HA$_{15}$ (0.91 A·mg^{-1}), Pt-Co/C-HA$_{60}$ (1.11 A·mg^{-1}), and commercialized Pt/C catalyst (0.27 A·mg^{-1}), respectively. From above results, it is obviously that constructing Pt-Co/CoO$_x$ can efficiently enhance the intrinsic activity of Pt based catalysts and promote HER process in alkaline electrolyte.

To deeply understanding the HER kinetics, the corresponding Tafel slopes are calculated and displayed in Fig. 4(c). The Pt-Co/C-HA$_{30}$ exhibited the best HER Tafel slope of 29.3 mV·dec^{-1}, which is markedly lower than Pt-Co/C-HA$_{60}$ (32.6 mV·dec^{-1}), Pt-Co/C-HA$_{15}$ (34.5 mV·dec^{-1}), Pt-Co/C-H (39.5 mV·dec^{-1}), and Pt/C (58.1 mV·dec^{-1}). Tafel slope below 30 mV·dec^{-1} reveals the substantially accelerated water dissociation kinetics on the Pt-Co/C-HA$_{30}$ and the Volmer step is no longer the rate-determining step (RDS) [50, 51]. Furthermore, such promotion on reaction kinetics was further confirmed by EIS. The charges transfer resistance (R_{ct}) of Pt-Co/C-H (47.05 Ω) was much lower than that of Pt/C (62.6 Ω), and the Pt-Co/CoO$_x$/C based electrocatalysts (Pt-Co/C-HA$_{15}$, Pt-Co/C-HA$_{30}$, and Pt-Co/C-HA$_{30}$) generally exhibited the lower charge transfer resistance (R_{ct}) than Pt-Co/C-H, as shown in Fig. 4(d). Moreover, the Pt-Co/C-HA$_{30}$ exhibits the lowest R_{ct} of 19.28 Ω among all catalysts. The detailed resistance of all catalysts is listed in the Table S5 in the ESM. Accordingly, it is clear that Pt-Co alloying and Pt-Co/CoO$_x$ interfacial construction both make great contribution to boost the kinetics in alkaline HER, and the interface constructed with amorphous CoO$_x$ will exhibit much stronger promotion than that of crystalline Co$_3$O$_4$.

As another vital parameter of electrocatalysis, the stability test of the Pt-Co/C-HA$_{30}$ catalyst was carried out by chronopotentiometry (Fig. 4(e)). Over the 24 h testing at the current density of 10 mA·cm^{-2}, no significant decline can be observed on Pt-Co/C-HA$_{30}$. Additionally, after the long-term cycling test of over 1,000 cyclins, no shift can be observed on the polarization curve of Pt-Co/C-HA$_{30}$. However, the Pt/C exhibits a significant degradation after the same cycling test. To directly visualize the strong stability of Pt-Co/C-HA$_{30}$, the TEM was applied to investigate the morphology after long-term OER test. Obviously, the uniform distribution of Pt-Co/CoO$_x$ NPs was well maintained without agglomeration, and the average particle size maintained at 2.46 nm (Fig. S4 in the ESM). Meanwhile, there was no significant increase in particle size, and also exhibiting the clear Pt-Co/CoO$_x$ interfacial structure. These observations indicate the excellent stability of the Pt-Co/C-HA$_{30}$ catalyst during the alkaline HER process.

To clarify the effect of PtCo/CoO$_x$ interfacial construction on alkaline HER catalysis, the Pt-Co/C-HA$_{30}$ was treated in the 1 M HCl to remove the surficial CoO$_x$, and investigated the HER property. After the removal of CoO$_x$ (Fig. S5 in the ESM), the Pt-Co/C-HA$_{30}$ indicates a significant decline on catalytic activity for alkaline HER (Fig. S6(a) in the ESM) with the overpotential increased from 28 to 41 mV at 10 mA·cm^{-2} (Fig. S6(b) in the ESM), and the Tafel slope increased from 29.3 to 41.7 mV·dec^{-1} (Fig. S6(c) in the ESM). Additionally, the charge transfer resistance increased from 19.28 to 30.25 Ω after acid treatment (Fig. S6(d) in the ESM), indicating the much lower charge transfer rate. Demonstrated by above results, the construction of Pt-Co/CoO$_x$ interface plays a vital role for the high alkaline HER activity of Pt-Co/C-HA$_{30}$.

3.3 Catalytic mechanism and DFT calculations

DFT calculations were further performed to further investigate the underlying catalytic mechanism of Pt-Co/CoO$_x$ interface. The constructed calculation models of Pt-Co and Pt-Co/CoO$_x$ were displayed in Figs. S7 and S8 in the ESM. To investigate the effect of Pt-Co/CoO$_x$ interface on electronic structure, different charge density of Pt-Co/CoO$_x$ was exhibited. The electrons flowed from Pt to Co, and resulted in the electron accumulation at the interfacial Co atom between the Pt-Co and CoO$_x$ in Fig. 5(a). The presence of electron-enriched state facilitates the water molecule adsorbing on interfacial Co atom, and makes it act as active sites for water dissociation [52, 53]. The electronic regulation by interfacial construction was also verified in PDOS (Fig. 5(b)). The d-band center of Pt in Pt-Co/CoO$_x$ was −2.108 eV, lower than that in Pt-Co (−1.969 eV). Meanwhile, the d-band center of Co also showed a negatively shifted from −0.9575 to −1.101 eV. The downshift of d band of both Pt and Co resulted in the optimized adsorption energies for H_2O and H*, which accelerate the sluggish alkaline HER [54, 55]. Moreover, the Pt-Co/CoO$_x$ also exhibited a higher occupy at Fermi level than that of Pt-Co (Fig. S9 in the ESM), indicating a higher electronic conductivity. Furthermore, the Gibbs free energy for water dissociation was calculated to directly determine the intrinsic activity for RDS in alkaline HER, and the three basic steps of water dissociation were all proceed on the interfacial Co sites in Pt-Co/CoO$_x$ and exterior Co sites in Pt-Co, respectively. As shown in the free energy diagram of water dissociation (Fig. 5(c)), the Gibbs free energy of water adsorption ($\Delta G_{H_2O^*}$) on Pt-Co/CoO$_x$ (−0.99 eV) is much lower than Pt-Co (−0.70 eV), indicating a more spontaneous water adsorption process on Pt-Co/CoO$_x$. For the following water dissociation step, the Pt-Co/CoO$_x$ also shows a reduced energy barrier of 0.70 eV, which is 0.04 eV lower than that of Pt-Co. Additionally, the Gibbs

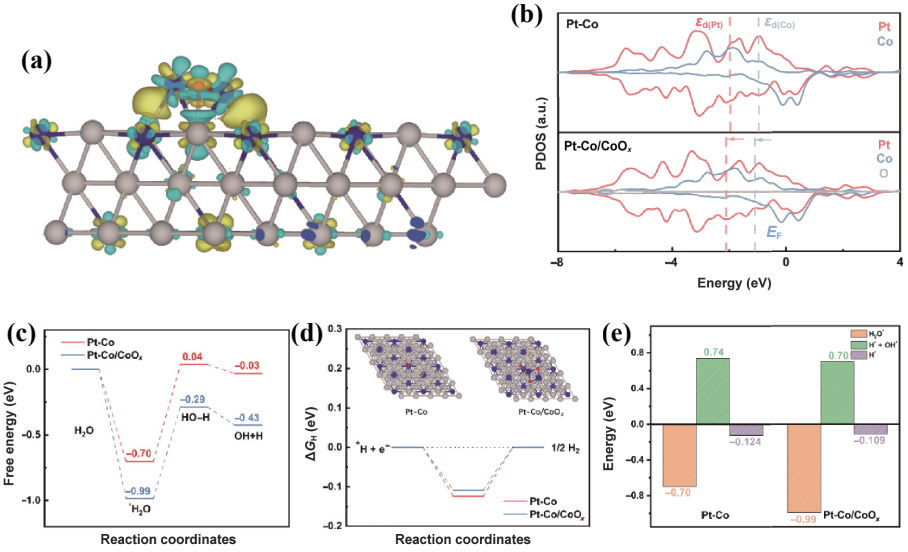

Figure 5 (a) Side view of different charge density distribution of Pt-Co/CoO$_x$, the yellow represents the charge accumulation, the cyan represents the charge depletion. (b) PDOS of Pt-Co and Pt-Co/CoO$_x$. (c) Reaction energy diagram of water dissociation. (d) The hydrogen absorption Gibbs free energy, insets: schematic illustration of H absorption. (e) The free energy of H_2O^*, H^*+OH^*, and H^*.

free energy of adsorbed hydrogen(ΔG_H) was also calculated. In the Pt-Co/Co$_x$, the Pt atom nearby the interfacial Co site was selected as active site for H* adsorption/desorption, while the Pt-Co selecting the exterior Pt atom. As shown in Fig. 5(d), the ΔG_H value of Pt-Co/CoO$_x$ (−0.109 eV) is closer to the thermal neutral position (zero) compared to Pt-Co (−0.124 eV). It indicates that the interface between Pt-Co and CoO$_x$ modulates the adsorbed H* closer to the zero, indicating a promoting H* adsorption/desorption process [56, 57]. Obviously, the Gibbs free energy for water adsorption, water dissociation and H* adsorption/desorption can all be reduced by constructing the Pt-Co/CoO$_x$ interface (Fig. 5(e)), resulting in a boosted HER kinetics in alkaline electrolyte.

4 Conclusion

In summary, by annealing Pt-Co/C in the air and controlling the heating time, we *in-situ* construct Pt-Co/CoO$_x$ interface on the carbon powders. Arising from the strong electronic interaction between Pt-Co and amorphous CoO$_x$, electron-enriched interfacial Co site is obtained and acts as the active sites for water dissociation. Besides, the electronic structure of Pt atoms and Co atoms can also be regulated by the construction of Pt-Co/CoO$_x$ interface, and exhibits the optimized Gibbs free energy for water adsorption, water dissociation, and hydrogen adsorption/desorption. Accordingly, the Pt-Co/C-HA$_{30}$ exhibits an overpotential of 28 mV at 10 mV·cm^{-2} and Tafel slope of 29.3 mV·dec^{-1} in 1 M KOH. Our work provides an effective approach to facilitating the water dissociation process by constructing interfacial structure with amorphous oxide cobalt, and achieving the highly efficient Pt based catalysts for alkaline HER.

Acknowledgements

This work was supported by the National Natural Science Foundation of China (No. 21875039), the Project on the Integration of Industry-Education-Research of Fujian Province (No. 2021H6020), and Fujian province's high level innovative and entrepreneurial talents (No. 50012709).

Electronic Supplementary Material: Supplementary material (TEM, mass activity, turnover frequency, acid treatment, calculation model diagram, reaction path model diagram, TDOS, d-band center pattern, and XPS value) is available in the online version of this article at https://doi.org/10.1007/s12274-022-4128-6.

References

[1] Yang, J. R.; Li, W. H.; Tan, S. D.; Xu, K. N.; Wang, Y.; Wang, D. S.; Li, Y. D. The electronic metal-support interaction directing the design of single atomic site catalysts: Achieving high efficiency towards hydrogen evolution. *Angew. Chem., Int. Ed.* **2021**, *60*, 19085–19091.

[2] He, Q.; Tian, D.; Jiang, H. L.; Cao, D. F.; Wei, S. Q.; Liu, D. B.; Song, P.; Lin, Y.; Song, L. Achieving efficient alkaline hydrogen evolution reaction over a Ni_5P_4 catalyst incorporating single-atomic Ru sites. *Adv. Mater.* **2020**, *32*, 1906972.

[3] Zhang, B.; Zhang, L. S.; Tan, Q. Y.; Wang, J. S.; Liu, J.; Wan, H. Z.; Miao, L.; Jiang, J. J. Simultaneous interfacial chemistry and inner Helmholtz plane regulation for superior alkaline hydrogen evolution. *Energy Environ. Sci.* **2020**, *13*, 3007–3013.

[4] Xie, L. B.; Wang, L. L.; Zhao, W. W.; Liu, S. J.; Huang, W.; Zhao, Q. WS_2 moiré superlattices derived from mechanical flexibility for hydrogen evolution reaction. *Nat. Commun.* **2021**, *12*, 5070.

[5] Lin, C. X.; Huang, Z. Q.; Zhang, Z. Y.; Zeng, T.; Chen, R. Z.; Tan, Y. Y.; Wu, W.; Mu, S. C.; Cheng, N. C. Structurally ordered Pt_3Co nanoparticles anchored on n-doped graphene for highly efficient hydrogen evolution reaction. *ACS Sustainable Chem. Eng.* **2020**, *8*, 16938–16945.

[6] Li, Z.; Feng, Y.; Liang, Y. L.; Cheng, C. Q.; Dong, C. K.; Liu, H.; Du, X. W. Stable rhodium (IV) oxide for alkaline hydrogen evolution reaction. *Adv. Mater.* **2020**, *32*, 1908521.

[7] Pu, Z. H.; Amiinu, I. S.; Cheng, R. L.; Wang, P. Y.; Zhang, C. T.; Mu, S. C.; Zhao, W. Y.; Su, F. M.; Zhang, G. X.; Liao, S. J. et al. Single-atom catalysts for electrochemical hydrogen evolution reaction: Recent advances and future perspectives. *Nano-Micro Lett.* **2020**, *12*, 21.

[8] Tan, Y. S.; Xie, R. K.; Zhao, S. Y.; Lu, X. K.; Liu, L. X.; Zhao, F. J.; Li, C. Z.; Jiang, H.; Chai, G. L.; Brett, D. J. L. et al. Facile fabrication of robust hydrogen evolution electrodes under high current densities via Pt@Cu interactions. *Adv. Funct. Mater.* **2021**, *31*, 2105579.

[9] Lu, J. J.; Zhang, L. S.; Jing, S. Y.; Luo, L.; Yin, S. B. Remarkably efficient PtRh alloyed with nanoscale WC for hydrogen evolution in alkaline solution. *Int. J. Hydrogen Energy* **2017**, *42*, 5993–5999.

[10] Cai, H. R.; Xiong, L. F.; Wang, B.; Zhu, D. L.; Hao, H. J.; Yu, X. J.; Li, C.; Yang, S. C. N-doped CNT as electron transport promoter by bridging CoP and carbon cloth toward enhanced alkaline hydrogen evolution. *Chem. Eng. J.* **2022**, *430*, 132824.

[11] Zhu, J.; Hu, L. S.; Zhao, P. X.; Lee, L. Y. S.; Wong, K. Y. Recent

advances in electrocatalytic hydrogen evolution using nanoparticles. *Chem. Rev.* **2020**, *120*, 851–918.

[12] Lu, Z. J.; Cao, Y. L.; Xie, J.; Hu, J. D.; Wang, K.; Jia, D. Z. Construction of Co_2P/CoP@Co@NCNT rich-interface to synergistically promote overall water splitting. *Chem. Eng. J.* **2022**, *430*, 132877.

[13] Chen, Q.; Wei, B.; Wei, Y.; Zhai, P. B.; Liu, W.; Gu, X. K.; Yang, Z. L.; Zuo, J. H.; Zhang, R. F.; Gong, Y. J. Synergistic effect in ultrafine PtNiP nanowires for highly efficient electrochemical hydrogen evolution in alkaline electrolyte. *Appl. Catal. B Environ.* **2022**, *301*, 120754.

[14] Lee, H.; Lim, J.; Lee, C.; Back, S.; An, K.; Shin, J. W.; Ryoo, R.; Jung, Y.; Park, J. Y. Boosting hot electron flux and catalytic activity at metal–oxide interfaces of PtCo bimetallic nanoparticles. *Nat. Commun.* **2018**, *9*, 2235.

[15] Wang, Y. J.; Zhao, N. N.; Fang, B. Z.; Li, H.; Bi, X. T.; Wang, H. J. Carbon-supported Pt-based alloy electrocatalysts for the oxygen reduction reaction in polymer electrolyte membrane fuel cells: Particle size, shape, and composition manipulation and their impact to activity. *Chem. Rev.* **2015**, *115*, 3433–3467.

[16] Wang, H. Q.; Zhang, W. J.; Zhang, X. W.; Hu, S. X.; Zhang, Z. C.; Zhou, W. J.; Liu, H. Multi-interface collaboration of graphene cross-linked NiS-NiS_2-Ni_3S_4 polymorph foam towards robust hydrogen evolution in alkaline electrolyte. *Nano Res.* **2021**, *14*, 4857–4864.

[17] Zhang, C. T.; Liu, Q.; Wang, P. Y.; Zhu, J. W.; Chen, D.; Yang, Y.; Zhao, Y. F.; Pu, Z. H.; Mu, S. C. Molybdenum carbide-PtCu nanoalloy heterostructures on MOF-derived carbon toward efficient hydrogen evolution. *Small* **2021**, *17*, 2104241.

[18] Zhao, Z. P.; Liu, H. T.; Gao, W. P.; Xue, W.; Liu, Z. Y.; Huang, J.; Pan, X. Q.; Huang, Y. Surface-engineered PtNi-O nanostructure with record-high performance for electrocatalytic hydrogen evolution reaction. *J. Am. Chem. Soc.* **2018**, *140*, 9046–9050.

[19] Wang, Z. Q.; Ren, X.; Luo, Y. L.; Wang, L.; Cui, G. W.; Xie, F. Y.; Wang, H. J.; Xie, Y.; Sun, X. P. An ultrafine platinum-cobalt alloy decorated cobalt nanowire array with superb activity toward alkaline hydrogen evolution. *Nanoscale* **2018**, *10*, 12302–12307.

[20] Xu, W. J.; Chang, J. F.; Cheng, Y. G.; Liu, H. Q.; Li, J. F.; Ai, Y. J.; Hu, Z. A.; Zhang, X. Y.; Wang, Y. M.; Liang, Q. L. et al. A multi-step induced strategy to fabricate core-shell Pt-Ni alloy as symmetric electrocatalysts for overall water splitting. *Nano Res.* **2022**, *15*, 965–971.

[21] Wang, P. T.; Shao, Q.; Guo, J.; Bu, L. Z.; Huang, X. Q. Promoting alkaline hydrogen evolution catalysis on p-decorated, Ni-segregated Pt-Ni-P nanowires via a synergetic cascade route. *Chem. Mater.* **2020**, *32*, 3144–3149.

[22] Shen, L. F.; Lu, B. A.; Li, Y. Y.; Liu, J.; Huang-Fu, Z. C.; Peng, H.; Ye, J. Y.; Qu, X. M.; Zhang, J. M.; Li, G. et al. Interfacial structure of water as a new descriptor of the hydrogen evolution reaction. *Angew. Chem., Int. Ed.* **2020**, *59*, 22397–22402.

[23] Yin, H. J.; Zhao, S. L.; Zhao, K.; Muqsit, A.; Tang, H. J.; Chang, L.; Zhao, H. J.; Gao, Y.; Tang, Z. Y. Ultrathin platinum nanowires grown on single-layered nickel hydroxide with high hydrogen evolution activity. *Nat. Commun.* **2015**, *6*, 6430.

[24] Qin, R.; Hou, J. G.; Xu, C. X.; Yang, H. X.; Zhou, Q. X.; Chen, Z. Z.; Liu, H. Self-supporting $Co_{0.85}Se$ nanosheets anchored on Co plate as highly efficient electrocatalyst for hydrogen evolution reaction in both acidic and alkaline media. *Nano Res.* **2020**, *13*, 2950–2957.

[25] Wang, Y.; Zheng, X. B.; Wang, D. S. Design concept for electrocatalysts. *Nano Res*. in press, https://doi.org/10.1007/s12274-021-3794-0.

[26] Wang, P. T.; Jiang, K. Z.; Wang, G. M.; Yao, J. L.; Huang, X. Q. Phase and interface engineering of platinum–nickel nanowires for efficient electrochemical hydrogen evolution. *Angew. Chem., Int. Ed.* **2016**, *55*, 12859–12863.

[27] Yu, X. W.; dos Santos, E. C.; White, J.; Salazar-Alvarez, G.; Pettersson, L. G. M.; Cornell, A.; Johnsson, M. Electrocatalytic glycerol oxidation with concurrent hydrogen evolution utilizing an efficient MoO_x/Pt catalyst. *Small* **2021**, *17*, 2104288.

[28] Zhou, M.; Li, H. F.; Long, A. C.; Zhou, B.; Lu, F.; Zhang, F. C.; Zhan, F.; Zhang, Z. X.; Xie, W. W.; Zeng, X. H. et al. Modulating 3d orbitals of Ni atoms on Ni-Pt edge sites enables highly-efficient alkaline hydrogen evolution. *Adv. Energy Mater.* **2021**, *11*, 2101789.

[29] Zhang, J. K.; Gao, Z.; Wang, S.; Wang, G. F.; Gao, X. F.; Zhang, B. Y.; Xing, S. F.; Zhao, S. C.; Qin, Y. Origin of synergistic effects in bicomponent cobalt oxide-platinum catalysts for selective hydrogenation reaction. *Nat. Commun.* **2019**, *10*, 4166.

[30] Liu, Z.; Zhang, C. Z.; Liu, H.; Feng, L. G. Efficient synergism of $NiSe_2$ nanoparticle/NiO nanosheet for energy-relevant water and urea electrocatalysis. *Appl. Catal. B Environ.* **2020**, *276*, 119165.

[31] Xu, Q. L.; Yu, T. Q.; Chen, J. L.; Qian, G. F.; Song, H. N.; Luo, L.; Chen, Y. L.; Liu, T. Y.; Wang, Y. Z.; Yin, S. B. Coupling interface constructions of $FeNi_3$-MoO_2 heterostructures for efficient urea oxidation and hydrogen evolution reaction. *ACS Appl. Mater. Interfaces* **2021**, *13*, 16355–16363.

[32] Zhang, W.; Jiang, X.; Dong, Z. M.; Wang, J.; Zhang, N.; Liu, J.; Xu, G. R.; Wang, L. Porous Pd/$NiFeO_x$ nanosheets enhance the pH-universal overall water splitting. *Adv. Funct. Mater.* **2021**, *31*, 2107181.

[33] Zeng, J. S.; Zhang, L.; Zhou, Q.; Liao, L. L.; Qi, Y.; Zhou, H. Q.; Li, D. Y.; Cai, F. M.; Wang, H.; Tang, D. S. et al. Boosting alkaline hydrogen and oxygen evolution kinetic process of tungsten disulfide-based heterostructures by multi-site engineering. *Small* **2022**, *18*, 2104624.

[34] Lim, J.; Jung, J. W.; Kim, N. Y.; Lee, G. Y.; Lee, H. J.; Lee, Y.; Choi, D. S.; Yoon, K. R.; Kim, Y. H.; Kim, I. D. et al. O. N_2-dopant of graphene with electrochemically switchable bifunctional ORR/OER catalysis for Zn–air battery. *Energy Storage Mater.* **2020**, *32*, 517–524.

[35] Yang, Y. M.; Ji, Y. J.; Li, G. Y.; Li, Y. Y.; Jia, B. H.; Yan, J. Q.; Ma, T. Y.; Liu, S. Z. F. IrO_x@In_2O_3 heterojunction from individually crystallized oxides for weak-light-promoted electrocatalytic water oxidation. *Angew. Chem., Int. Ed.* **2021**, *60*, 26790–26797.

[36] Yan, Y.; Liang, S.; Wang, X.; Zhang, M. Y.; Hao, S. M.; Cui, X.; Li, Z.; Lin, Z. Q. Robust wrinkled MoS_2/N-C bifunctional electrocatalysts interfaced with single Fe atoms for wearable zinc–air batteries. *Proc. Natl. Acad. Sci. USA* **2021**, *118*, e2110036118.

[37] Zhang, J.; Zhang, Q. Y.; Feng, X. L. Support and interface effects in water-splitting electrocatalysts. *Adv. Mater.* **2019**, *31*, 1808167.

[38] Wu, D. L.; Chen, D.; Zhu, J. W.; Mu, S. C. Ultralow Ru incorporated amorphous cobalt-based oxides for high-current-density overall water splitting in alkaline and seawater media. *Small* **2021**, *17*, 2102777.

[39] Xu, L.; Tian, Y. H.; Deng, D. J.; Li, H. P.; Zhang, D.; Qian, J. C.; Wang, S.; Zhang, J. M.; Li, H. N.; Sun, S. H. Cu nanoclusters/FeN_4 amorphous composites with dual active sites in N-doped graphene for high-performance Zn–air batteries. *ACS Appl. Mater. Interfaces* **2020**, *12*, 31340–31350.

[40] Wu, M. J.; Wei, Q. L.; Zhang, G. X.; Qiao, J. L.; Wu, M. X.; Zhang, J. H.; Gong, Q. J.; Sun, S. H. Fe/Co double hydroxide/oxide nanoparticles on N-doped CNTs as highly efficient electrocatalyst for rechargeable liquid and quasi-solid-state zinc–air batteries. *Adv. Energy Mater.* **2018**, *8*, 1801836.

[41] Hua, B.; Li, M.; Sun, Y. F.; Zhang, Y. Q.; Yan, N.; Chen, J.; Thundat, T.; Li, J.; Luo, J. L. A coupling for success: Controlled growth of Co/CoO_x nanoshoots on perovskite mesoporous nanofibres as high-performance trifunctional electrocatalysts in alkaline condition. *Nano Energy* **2017**, *32*, 247–254.

[42] Anantharaj, S.; Noda, S. Amorphous catalysts and electrochemical water splitting: An untold story of harmony. *Small* **2020**, *16*, 1905779.

[43] Yu, T. Q.; Xu, Q. L.; Qian, G. F.; Chen, J. L.; Zhang, H.; Luo, L.; Yin, S. B. Amorphous CoO_x-decorated crystalline RuO_2 nanosheets as bifunctional catalysts for boosting overall water splitting at large current density. *ACS Sustainable Chem. Eng.* **2020**, *8*, 17520–17526.

[44] Jiang, L. H.; Sun, G. Q.; Zhou, Z. H.; Zhou, W. J.; Xin, Q. Preparation and characterization of PtSn/C anode electrocatalysts for direct ethanol fuel cell. *Catal. Today* **2004**, *93–95*, 665–670.

[45] Jiang, L. H.; Zhou, Z. H.; Li, W. Z.; Zhou, W. J.; Song, S. Q.; Li, H. Q.; Sun, G. Q.; Xin, Q. Effects of treatment in different atmosphere on Pt_3Sn/C electrocatalysts for ethanol electro-oxidation. *Energy*

Fuels **2004**, *18*, 866–871.

[46] Cui, C. H.; Gan, L.; Heggen, M.; Rudi, S.; Strasser, P. Compositional segregation in shaped Pt alloy nanoparticles and their structural behaviour during electrocatalysis. *Nat. Mater.* **2013**, *12*, 765–771.

[47] Jang, S. W.; Dutta, S.; Kumar, A.; Hong, Y. R.; Kang, H.; Lee, S.; Ryu, S.; Choi, W.; Lee, I. S. Holey Pt nanosheets on NiFe-hydroxide laminates: Synergistically enhanced electrocatalytic 2D interface toward hydrogen evolution reaction. *ACS Nano* **2020**, *14*, 10578–10588.

[48] Wang, M. J.; Xu, Y.; Peng, C. K.; Chen, S. Y.; Lin, Y. G.; Hu, Z. W.; Sun, L.; Ding, S. Y.; Pao, C. W.; Shao, Q. et al. Site-specified two-dimensional heterojunction of Pt nanoparticles/metal–organic frameworks for enhanced hydrogen evolution. *J. Am. Chem. Soc.* **2021**, *143*, 16512–16518.

[49] Chen, W. S; Xue, J.; Bao, Y. F.; Feng, L. G. Surface engineering of nano-ceria facet dependent coupling effect on Pt nanocrystals for electro-catalysis of methanol oxidation reaction. *Chem. Eng. J.* **2020**, *381*, 122752.

[50] Xie, Y. F.; Cai, J. Y.; Wu, Y. S.; Zang, Y. P.; Zheng, X. S.; Ye, J.; Cui, P. X.; Niu, S. W.; Liu, Y.; Zhu, J. F. et al. Boosting water dissociation kinetics on Pt-Ni nanowires by N-induced orbital tuning. *Adv. Mater.* **2019**, *31*, 1807780.

[51] Chen, J. L.; Qian, G. F.; Zhang, H.; Feng, S. Q.; Mo, Y. S.; Luo, L.; Yin, S. B. PtCo@PtSn heterojunction with high stability/activity for pH-universal H_2 evolution. *Adv. Funct. Mater.* **2021**, 2107597.

[52] Hu, S.; Goenaga, G.; Melton, C.; Zawodzinski, T. A.; Mukherjee, D. PtCo/CoO_x nanocomposites: Bifunctional electrocatalysts for oxygen reduction and evolution reactions synthesized via tandem laser ablation synthesis in solution-galvanic replacement reactions. *Appl. Catal. B Environ.* **2016**, *182*, 286–296.

[53] Lu, Z. J.; Xie, J.; Hu, J. D.; Wang, K.; Cao, Y. L. *In situ* replacement synthesis of Co@NCNT encapsulated $CoPt_3$@Co_2P heterojunction boosting methanol oxidation and hydrogen evolution. *Small* **2021**, *17*, 2104656.

[54] Yang, G. C.; Jiao, Y. Q.; Yan, H. J.; Xie, Y.; Wu, A. P.; Dong, X.; Guo, D. Z.; Tian, C. G.; Fu, H. G. Interfacial engineering of MoO_2-FeP heterojunction for highly efficient hydrogen evolution coupled with biomass electrooxidation. *Adv. Mater.* **2020**, *32*, 2000455.

[55] Sun, Y. M.; Xue, Z. Q.; Liu, Q. L.; Jia, Y. L.; Li, Y. L.; Liu, K.; Lin, Y. Y.; Liu, M.; Li, G. Q.; Su, C. Y. Modulating electronic structure of metal–organic frameworks by introducing atomically dispersed Ru for efficient hydrogen evolution. *Nat. Commun.* **2021**, *12*, 1369.

[56] Zhang, L. J.; Jang, H.; Wang, Y.; Li, Z. J.; Zhang, W.; Kim, M. G.; Yang, D. J.; Liu, S. G.; Liu, X. E.; Cho, J. Exploring the dominant role of atomic- and nano-ruthenium as active sites for hydrogen evolution reaction in both acidic and alkaline media. *Adv. Sci.* **2021**, *8*, 2004516.

[57] Zhang, D. D.; Li, H. B.; Riaz, A.; Sharma, A.; Liang, W. S.; Wang, Y.; Chen, H. J.; Vora, K.; Yan, D.; Su, Z. et al. Unconventional direct synthesis of Ni_3N/Ni with N-vacancies for efficient and stable hydrogen evolution. *Energy Environ. Sci.*, in press, https://doi.org/10.1039/D1EE02013G.